Power balance analysis experiments on an axisymmetric fuselage with an integrated boundary-layer-ingesting fan

Corte, Biagio Della; van Sluis, Martijn; Veldhuis, Leo L.M.; Rao, Arvind Gangoli

DOI
10.2514/1.J060570

Publication date
2021

Document Version
Final published version

Published in
AIAA Journal

Citation (APA)
Corte, B. D., van Sluis, M., Veldhuis, L. L. M., & Rao, A. G. (2021). Power balance analysis experiments on an axisymmetric fuselage with an integrated boundary-layer-ingesting fan. *AIAA Journal*, *59*(12), 5211-5224. https://doi.org/10.2514/1.J060570

AIAA JOURNAL
Vol. 59, No. 12, December 2021

Power Balance Analysis Experiments on an Axisymmetric Fuselage with an Integrated Boundary-Layer-Ingesting Fan

Biagio Della Corte,* Martijn van Sluis,† Leo L. M. Veldhuis,‡ and Arvind Gangoli Rao§
Delft University of Technology, 2629 HS Delft, The Netherlands

https://doi.org/10.2514/1.J060570

Boundary Layer Ingestion (BLI) is a promising propulsion integration technology capable of enhancing aircraft propulsive efficiency. The Propulsive Fuselage Concept (PFC), a tube-and-wing configuration with an aft-fuselage-mounted BLI propulsor, is particularly suited for BLI. Although extensively studied on a system level, the aerodynamic performance of the PFC, resulting from the complex interaction between the airframe and the propulsor, is still largely uncharted. In this paper, the results of wind-tunnel tests on a simplified PFC model are presented. The model featured an axisymmetric fuselage body with an integrated BLI shrouded fan. Flowfield measurements were performed through particle image velocimetry to analyze the key aerodynamic phenomena and to assess the distribution of momentum and mechanical energy around the aft-fuselage propulsor. Results show that the BLI fan alters the surrounding flowfield by increasing the mass flow in the inner part of the fuselage boundary layer and by reducing the boundary-layer thickness. Moreover, the power analysis indicates that the potential benefit of BLI is strongly dependent on the fan setting. Increasing the fan shaft power leads to a higher amount of power dissipated in the near wake. However, an increasing share of the energy flux is associated with the momentum excess contained in the wake.

Nomenclature

C_{D_0}	=	bare fuselage drag coefficient
$C_{\dot{E}_a}$	=	axial kinetic energy deposition rate coefficient
$C_{\dot{E}_p}$	=	pressure work rate coefficient
$C_{\dot{E}_r}$	=	radial kinetic energy deposition rate coefficient
$C_{\dot{E}_t}$	=	tangential kinetic energy deposition rate coefficient
$C_{\dot{E}_\kappa}$	=	turbulence kinetic energy deposition rate coefficient
$C_{\dot{E}}$	=	kinetic energy deposition rate coefficient
C_{F_x}	=	axial momentum flux coefficient
C_N	=	net axial force coefficient
C_{P_k}	=	propulsor mechanical power input coefficient
C_{p_t}	=	total pressure coefficient
C_p	=	static pressure coefficient
$C_{\dot{e}}$	=	total mechanical power outflow coefficient
C_ϕ	=	viscous dissipation rate coefficient
L_b	=	fuselage body length, m
M	=	Mach number
n	=	boundary-normal direction
p	=	static pressure, Pa
p_t	=	total pressure, Pa
q	=	dynamic pressure, Pa
R_b	=	fuselage body radius, m
R_f	=	fan radius, m
Re	=	Reynolds number
Re_{L_b}	=	fuselage length-based Reynolds number
S_{ref}	=	reference area, m^2
S_{TS}	=	wind-tunnel test-section cross-sectional area, m^2
s	=	wall-normal distance, m
U, V, W	=	Cartesian components of $\boldsymbol{V}$, m/s
U_{tip}	=	fan tip speed, m/s
u, v, w	=	Cartesian components of $\boldsymbol{V} - \boldsymbol{V}_\infty$, m/s
u_t, u_n	=	wall-tangential and wall-normal components of $\boldsymbol{V} - \boldsymbol{V}_\infty$, m/s
$\boldsymbol{V}$	=	velocity vector, m/s
x, r, θ	=	cylindrical coordinates
x, y, z	=	Cartesian coordinates
δ_{99}	=	boundary-layer physical thickness, m
ϵ	=	uncertainty of particle image velocimetry measurements, m/s
κ	=	turbulence kinetic energy, $m^2 \cdot s^2$
μ	=	air dynamic viscosity, Pa · s
ρ	=	air density, kg/m^3
σ	=	standard deviation of particle image velocimetry measurements
Ω	=	fan angular velocity, rad/s
ω_x	=	axial vorticity, 1/s

Subscript

∞	=	freestream conditions

Received 22 January 2021; revision received 6 May 2021; accepted for publication 13 May 2021; published online Open Access 11 October 2021.

*Ph.D. Candidate, Faculty of Aerospace Engineering, Flight Performance and Propulsion Group; b.dellacorte@tudelft.nl.

†Researcher, Faculty of Aerospace Engineering, Flight Performance and Propulsion Group.

‡Full Professor, Section Head, Faculty of Aerospace Engineering, Flight Performance and Propulsion Group.

§Associate Professor, Flight Performance and Propulsion Group, Faculty of Aerospace Engineering; a.gangolirao@tudelft.nl.

I. Introduction

BOUNDARY Layer Ingestion (BLI) can enhance the aerodynamic and propulsive efficiency of aircraft systems, promising significant power saving benefits for future aviation. The propulsive efficiency benefit achieved by operating a propeller in the wake of a body has long been known and it was firstly theorized by Betz [1]. A milestone theoretical study on a wake-ingesting propeller related the boundary-layer integral properties to those of the propulsor to model the achieved power benefit [2]. A maximum propulsive benefit of 20% was estimated for the ideal wake ingestion case, where the propulsor is at the trailing edge of the body and its wake is fully recovered. Moreover, Ref. [2] was the first to discuss the ambiguity of the conventional thrust-drag bookkeeping and of the propulsive efficiency for the wake-ingesting propeller. Therefore, the power saving coefficient was proposed as an unambiguous performance metric for integrated configurations. In fact, conventional performance analysis based on the definition of thrust and drag is generally not suited for the analysis of a BLI configuration, because of the tight integration between the airframe and the propulsor [3]. On the

contrary, the power balance method (PBM) is based on the mechanical energy integral equation and it can be used to analyze integrated configurations without the need to decompose the forces into drag and thrust components [4]. Theoretical and numerical works applied the PBM on wake and boundary-layer ingestion, showing that the reason of the power benefit is twofold. First, the inlet kinetic energy associated with the ingested boundary layer represents a power input for the BLI propulsor. Second, the jet and wake viscous dissipation is reduced, by introducing energy and momentum in the ingested boundary layer instead of the freestream flow [5,6]. However, only the first mechanism was experimentally demonstrated for a wake-ingesting configuration [7].

In the last decade, BLI has been used in numerous aircraft design studies. Experimental and numerical studies estimated a power benefit of the order of 10% due to BLI for the MIT D8 aircraft [8,9]. Similarly, Reynolds-averaged Navier–Stokes (RANS) simulations showed a benefit of 5% for the Nextgen Onera Versatile Aircraf (NOVA) configuration proposed by ONERA [10]. Another example of blended wing–bodies featuring BLI can be found in the Silent Aircraft concept [11]. Among these configurations, the Propulsive Fuselage Concept (PFC) is one of the most promising BLI designs [12]. The PFC is a tube-and-wing aircraft where a BLI engine is integrated at the aft section of the fuselage body. The PFC has numerous advantages over other BLI concepts. First, the fuselage geometry is well-suited for a BLI propulsor that can possibly ingest the entire fuselage boundary layer. As a consequence, viscous losses in the wake can be minimized as a large portion of the airframe boundary layer can be energized [12]. In addition, the inflow distortion associated with the fuselage boundary layer could be axisymmetric. Therefore, this distortion would not induce any unsteady fan blade loading and the fan design can be adapted to minimize the fan installation penalty [13]. Finally, the PFC is a relatively conventional design that can ease the design and analysis while still providing a first step toward unconventional aircraft configurations. For these reasons, the PFC has attracted a broad interest in recent years. The DisPURSAL project studied a PFC aircraft with the fuselage fan powered through a gas turbine. A block fuel burn reduction of around 10% was estimated compared with an equivalent conventional design [14]. More recently, the EU-funded CENTRELINE project proposed a turbo-electric PFC design for a long-range passenger aircraft [15]. In cruise conditions, the electric-driven BLI fan has a power share equal to approximately 30% of the total propulsive power, leading to a power saving of around 5% over a conventional aircraft [16]. NASA investigated a similar PFC configuration named the STARC-ABL estimating similar power benefits [17].

The predicted aero-propulsive performance of the PFC relies on computational fluid dynamics (CFD) simulations where the BLI propulsor is often implemented through an actuator disk model [14–16,18–20]. This model does not capture the effects of the boundary-layer inflow on the fan performance, non-uniform blade, and disk loading and of the swirl in the propulsor slipstream. Previous experimental studies on the interaction between an axisymmetric fuselage and a downstream propeller focused on the wake-ingestion case, where the propulsor is placed far downstream of the body to avoid any pressure field interactions [7,21]. Recently, an experimental work on an axisymmetric-body with BLI proposed a benchmark for numerical modeling but did not investigate the aerodynamic field in great details [22]. Moreover, no examples of experimental implementation of the PBM on an axisymmetric BLI configuration are present in literature. For these reasons, the aerodynamics of BLI applied on a fuselage body is largely uncharted and needs to be studied with dedicated experimental investigations.

In this paper we discuss wind-tunnel experiments of a simplified PFC configuration featuring an axisymmetric fuselage with a BLI propulsor integrated with the fuselage aft section. The geometry of the aft fuselage section of the model is based on the PFC configuration proposed within the CENTRELINE project [16]. The shrouded fan was designed to match the aerodynamic performance of the CENTRELINE full-scale fan and the inflow boundary-layer properties [13]. The present study separated the main distortion component (fuselage boundary layer) from the secondary ones (wing and tail wakes), in an effort to obtain a direct measurement of the interaction between the fuselage boundary layer and the BLI fan. The PBM was applied on flowfield data measured with particle image velocimetry (PIV) to understand how momentum and mechanical energy were distributed in the boundary layer of the fuselage and how they were affected by the BLI fan setting.

II. Methods

The aim of the work presented is to investigate the fundamental aerodynamics of an axisymmetric BLI–fuselage configuration in symmetric flow conditions. To this end, low-speed wind-tunnel tests were employed to provide the relevant data. Given the scaling limitations, the Reynolds number and Mach number characterizing the wind-tunnel test did not match the expected full-flight-scale conditions (corresponding to a Reynolds number based on the fuselage length, Re_{L_b}, of 400×10^6 and a Mach number, M_∞, of 0.82). However, the obtained data are considered relevant for the understanding of the aerodynamics of fuselage–BLI for various reasons. First, the BLI propulsor model was scaled to match the fuselage boundary layer, which is relatively thicker because of the Reynolds number effects (see Sec. II.A.4). Second, previous work, e.g., Refs. [23–25], shows that the critical Mach number of axisymmetric bodies at zero incidence angles is higher than the typical commercial aviation cruise Mach number. As a consequence, compressibility effects are not expected to substantially affect the fuselage boundary layer.

A. Wind-Tunnel Facility and Model

1. Facility

The experiments were carried out at the Low Turbulence Tunnel (LTT) of Delft University of Technology. This facility is an atmospheric, closed-circuit wind tunnel with a closed test section. The freestream turbulence intensity level is about 0.02% for a freestream velocity within 10 and 40 m/s [26]. The test section features an octagonal cross section with a width of 1.8 m and a height of 1.25 m.

2. Model Setup

The tested model features an axisymmetric fuselage equipped with a shrouded fan integrated with the fuselage aft section. Photographs and technical drawings of the setup are presented in Figs. 1 and 2.

This setup has three main advantages: first, the effects of the fuselage boundary layer could be isolated from those of other inlet distortions sources, such as wing and tail surfaces; second, the fuselage boundary layer would produce, ideally, a purely radial distortion and an uniform blade loading, hence minimizing unsteady phenomena; finally, the forces acting on the fuselage–fan assembly could be directly measured by means of an external six-component balance. The fuselage and the shrouded fan were connected to the external balance through a support beam, housed inside the fairing on the upper side of the fuselage. A second fairing was mounted at the bottom of the setup to enhance the setup symmetries. The fairings were directly bolted to the test-section walls, and a gap of 1 mm ensured no contact with the fuselage model. Hence, only the fuselage and fan assembly were sensed by the external balance. This rendered unnecessary any tare procedure to remove the forces acting on the support structure from the total balance readings.

3. Fuselage Model

The axisymmetric fuselage body featured a radius R_b of 80 mm (at the central, cylindrical part) and a length L_b equal to 1776 mm. A turbulent boundary layer was ensured through zigzag turbulator tape with a slope of 60°, thickness of 0.4 mm, and width of 12 mm installed at $x/L_b = 5\%$. The effectiveness of the transition strips and the uniformity of the transition behavior around the entire fuselage contour were checked through the use of a stethoscope. The fuselage aft section could be arranged in two geometrical configurations, the bare fuselage (BF) and the powered fuselage (PF), sketched in Fig. 3. The BF configuration consisted of the baseline fuselage contour without the shrouded fan, whereas the PF configuration was obtained

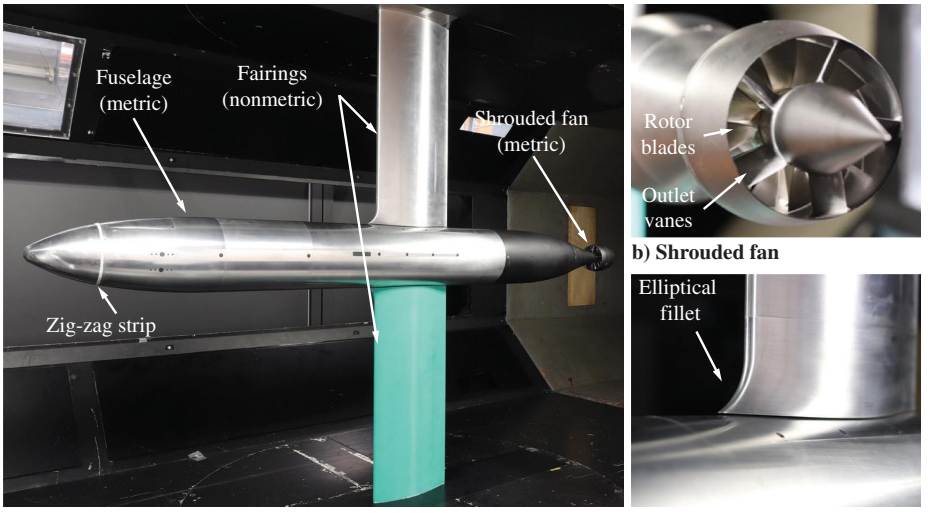

a) Isometric assembly view

b) Shrouded fan

c) Fairing-fuselage interface

Fig. 1 Wind-tunnel model setup used during the experiments in the Low Turbulence Tunnel of Delft University of Technology.

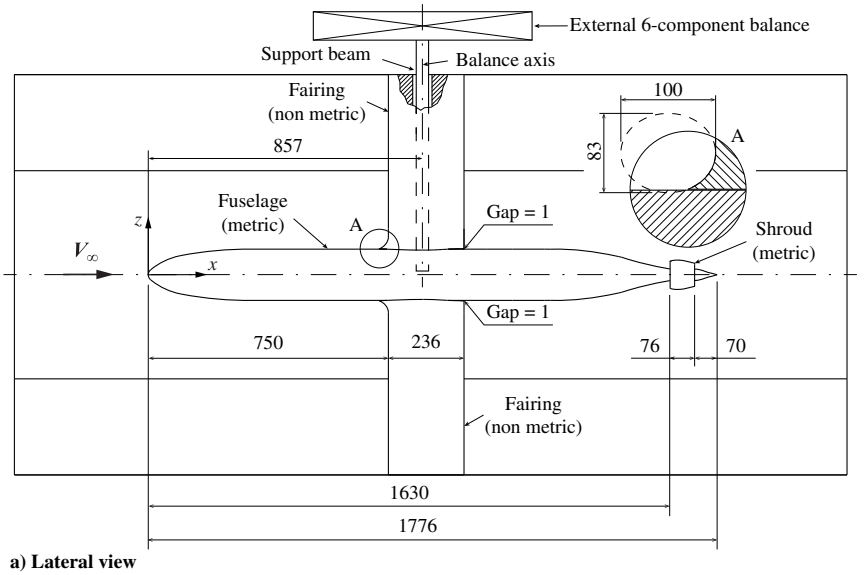

a) Lateral view

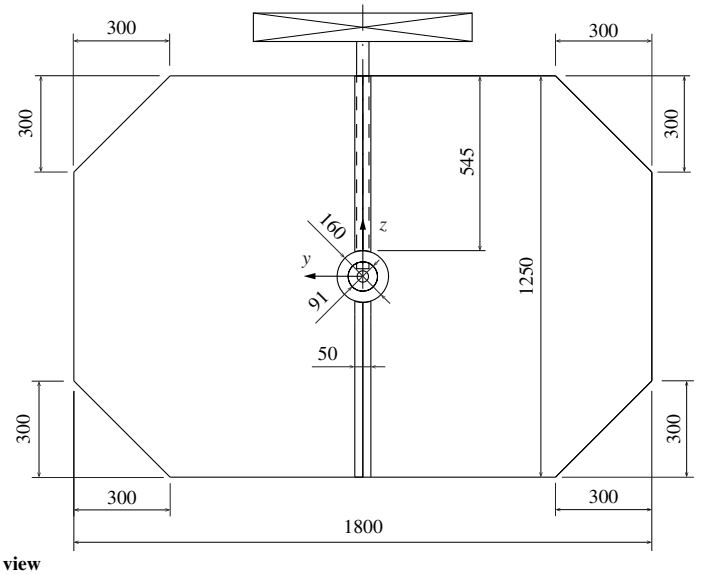

b) Back view

Fig. 2 Technical drawing of the wind-tunnel setup used during the experiments in the Low Turbulence Tunnel of Delft University of Technology. (Dimensions are in millimeters.)

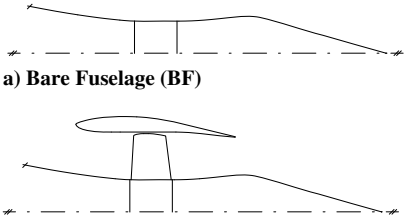

a) Bare Fuselage (BF)

b) Powered Fuselage (PF)

Fig. 3 Fuselage aft section geometrical configurations as tested in the wind-tunnel experiments.

by mounting the shrouded fan onto the BF. The aft-cone geometry was adapted from the design of the CENTRELINE PFC (see, e.g., [15,16]).

4. Fan and Shroud Model

The PF aft-cone was equipped with a shrouded fan, of which detail drawings are presented in Fig. 4. The fan was driven by a three-phase electric motor, housed inside the fuselage aft section. During the measurements, the fan angular velocity, Ω, was measured through an US Digital optical encoder mounted on the motor shaft. The fan model featured a 12-bladed rotor with a tip diameter, R_f, of 37.6 mm ($R_f/R_b = 0.47$). The hub radius was equal to 15.4 mm, resulting in a hub-to-tip radii ratio of 0.41 and a blade height of 22 mm.

The fan was sized to ensure aerodynamic similarity with the full-scale CENTRELINE PFC. Because of the differences in Reynolds and Mach numbers between the wind-tunnel scale and full-scale conditions, the boundary layer is expected to be larger relatively to the fuselage in the wind-tunnel test. Therefore, the fan diameter was adapted to the scaled boundary-layer thickness to achieve the same ratio of momentum thickness to fan blade height as the full-scale CENTRELINE configuration. The blade geometry was optimized at the same design point of the full-scale fuselage–fan, which is installed on the full-scale CENTRELINE PFC [13]. At the wind-tunnel scale, the design point was characterized by $U_{\text{tip}}/V_\infty = 1.64$, where V_∞ is the freestream velocity and $U_{\text{tip}} = \Omega R_f$ is the fan tip speed. A more detailed discussion of the design procedure can be found in Ref. [27].

The shroud contour was adapted from the CENTRELINE design. The tip gap was equal to 0.75 mm (approximately 1% of the fan tip diameter). The shroud inlet featured five inlet vanes, as shown in Fig. 4a. The inlet vanes featured a symmetric airfoil section with a rectangular planform. The vanes had a structural function and were not optimized to de-swirl the flow. Two shroud outlet configurations were tested: 1) one featuring five outlet vanes to which the nozzle plug was mounted (showed in Fig. 4b); 2) one without the outlet vanes, in which the nozzle plug was rotating integrally with the fan. The outlet vanes design (airfoil shape and blade geometry) was adapted to the measured swirl angle in the fan slipstream to avoid detrimental effects on the flowfield (e.g., flow separation on the outlet vanes). However, the outlet vanes were not optimized to completely recover the swirl in the fan slipstream.

5. Fairing Configuration

The fairings featured a NACA 66_4-021 airfoil section and a rectangular planform with a chord length of 236 mm. The inboard tip of the fairings featured a curved surface following the fuselage contour. A radial gap of 1 mm was ensured from the fuselage contour to avoid material contact. The inboard tips also featured an elliptical leading-edge fillet (see Fig. 1) to reduce the distortions introduced in the flow by the fairing. The bottom fairing did not have any structural function and was employed to reduce the effects of the fairings on the flowfield around the fuselage aft section. More details of the fairing design were presented in a previous related work [28].

B. Measurement Techniques

1. Balance Measurements

The external six-component balance was used to measure the aerodynamic forces and moments acting on the model. Because the fairings were directly bolted to the wind-tunnel walls and no material contact was allowed between the fairing and the fuselage, only the fuselage model was sensed by the balance. Therefore, the balance readings directly provided the net force acting on the fuselage–fan assembly. The measurements were averaged out over a time of at least 10 s to filter out fluctuations due to turbulence or vibrations. Force coefficients are computed using the freestream dynamic pressure, q_∞, and the fuselage surface frontal area, $S_{\text{ref}} = \pi R_b^2$, as reference values.

To assess the data uncertainty due to various error sources (e.g., random error, variations in ambient and freestream conditions, model surface contamination, turbulence fluctuations) the same measurements were replicated in various runs. A maximum deviation of 0.006 was found for the axial force coefficient C_N, approximately equal to 4% of the BF drag coefficient C_{D_0}.

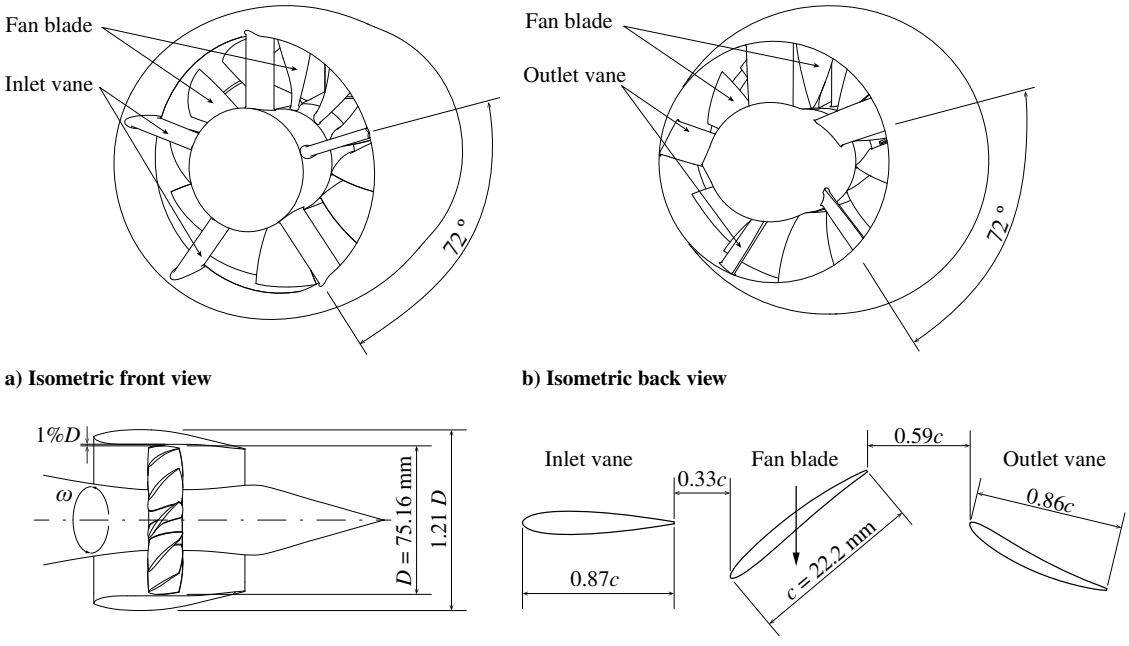

a) Isometric front view

b) Isometric back view

c) Section view

d) Cross-section at 50% span

Fig. 4 Detail drawings of the fuselage-mounted shrouded fan.

Because the focus of the balance measurements was to assess the effect of the BLI propulsor relatively to the bare configuration, wind-tunnel wall and model blockage corrections were not employed.

2. *Particle Image Velocimetry Measurements*

Stereoscopic particle image velocimetry (PIV) was used to measure the three velocity components in two different planes, which are shown in Fig. 5. Table 1 summarizes the main parameters of the two PIV setups. The wake-plane field of view (WP-FoV) shown in Fig. 5a, was orthogonal to the freestream velocity direction and placed at a distance of $1R_b$ from the fuselage trailing edge (corresponding to $x/L_b = 1.05$). The velocity data measured in this plane were used to obtain a 3-D wake analysis. In addition, the symmetry-plane field of view (SP-FoV) shown in Fig. 5b allowed a more detailed analysis of the flow around the fuselage propulsor. The velocity data obtained in the SP-FoV plane were used to analyze the momentum and mechanical energy distribution in the fuselage boundary layer and around the BLI propulsor.

For both planes, two LaVision Imager sCMOS cameras were used in a stereoscopic setup. These cameras feature a 16-bit 2560 px × 2160 px sensor and have a maximum acquisition frequency of 50 Hz. The cameras were equipped with Nikon 105 mm f/2.8 AF-D Micro Nikkor lenses and with LaVision Scheimpflug Adapters. During all the measurements, the aperture was set to f/8. The airflow was seeded with Safex Inside Nebelfluid and via a Safex Twin Fog smoke generator. Illumination was provided by a Quantel Evergreen double-pulse Nd:YAG laser. A laser sheet with a thickness of around 2.5 mm was obtained through standard laser optics.

Images acquisition was controlled via LaVision DaVis 8.4 software and synchronized via a LaVision USB Programmable Time Unit. The pulse separation was set in order to achieve a freestream particle displacement of around 10 px. For each case, sets of 1000–1500 image pairs were recorded at around 10 Hz. In cases with powered fan, the acquisition frequency was set to avoid phase-locking with the fan blades. Post-processing of particle images was also performed in LaVision DaVis 8.4 with an iterative multipass correlation algorithm with a decreasing window size [29]. For each case, the instantaneous vector fields were averaged to obtain the ensemble-average velocity measurement. For the SP-FoV case, the PIV setup (laser optics and cameras) was automatically translated in the axial direction thanks to an electronic traversing system. To obtain a sufficient spatial resolution in a large domain, the SP-FOV field was obtained by measuring the velocity in two coplanar domains. The two vector fields were subsequently stitched together.

The uncertainty of the PIV measurements was estimated for each measured vector during the correlation operation, using a statistical analysis of the image pair correlation results [30]. The uncertainty values for the average flowfield were obtained by averaging out the uncertainty fields of each instantaneous field. The maximum value of the uncertainty on the velocity magnitude and on each of the velocity components is reported in Table 1. The uncertainty was subtracted from the computation of turbulence statistics like the turbulence kinetic energy.

3. *Total Pressure Measurements*

Total pressure measurements were carried out in the wake of the model using a rake consisting of 44 total-pressure probes. The scanned plane coincided with the WP-FoV PIV plane of Fig. 5. The probes were non-evenly distributed with a minimum lateral spacing of 3 mm (equal to 3.75% of R_b) at the center of the rake. The rake was traversed in the vertical direction with a minimum step size of 0.5 mm (0.625% of R_b) at the fuselage center and gradually increasing at larger z positions (see Fig. 2). At each scanned position, total pressure measurements were acquired with an electronic pressure scanner for a period of 10 s and time-averaged to obtain each single data point. During each measurement, the freestream conditions were measured through a static Pitot probe positioned at the test-section inlet and recorded simultaneously using the same pressure scanner. Each wake-rake measurement was nondimensionalized with the corresponding freestream values to obtain the total pressure coefficient $C_{p_t} = (p_t - p_{t,\infty})/q_\infty$.

Table 1 Summary of the main parameters of the particle image velocimetry setups

Parameter	WP-FoV	SP-FoV
Imaging		
Focal length [mm]	105	105
Aperture	f/8	f/8
Digital resolution [px/mm]	12.08	12.20
Acquisition		
Pulse delay [μs]	20	10
Number of image pairs	>1000	1500
Processing		
Interrogation window [px × px]	32 × 32	24 × 24
Overlap factor [%]	50	75
Spatial resolution [mm]	0.25	0.40
Uncertainty		
u component uncertainty ϵ_u/V_∞ [%]	0.5	0.6
v component uncertainty ϵ_v/V_∞ [%]	0.6	0.8
w component uncertainty ϵ_w/V_∞ [%]	0.6	0.9
Velocity magnitude uncertainty ϵ_V/V_∞ [%]	0.9	1.1

C. Analyzed Cases

All the measurements were taken at symmetric inflow conditions, i.e., for a zero incidence angle. The freestream velocity V_∞ was varied from 15 to 40 m/s (corresponding to a Reynolds number based on the fuselage length, Re_{L_b}, between 1.7×10^6 and 4.7×10^6 and a freestream Mach number M_∞ between 0.04 and 0.12) in combination with the fan angular velocity, Ω, to control the operating fan tip speed ratio. In powered conditions, the ratio between the measured net axial force and drag of the BF was used as an independent parameter to characterize the operating condition.

D. PIV-Based Momentum and Power Analysis

The Power Balance Method (PBM) [4] was applied to the PIV data obtained in the SP-FoV. Figure 6 shows a sketch of the domain and notations defined for the analysis.

1. *Pressure Reconstruction*

The static pressure field was inferred from the PIV data by solving the Poisson equation for the pressure (see, e.g., [31] for a review of the

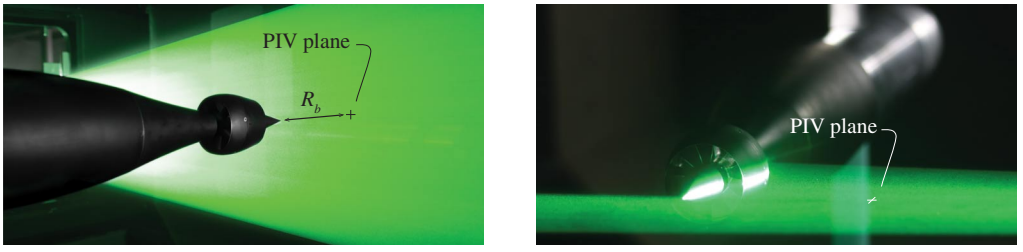

a) Wake-Plane Field of View (WP-FoV) **b) Symmetry-Plane Field of View (SP-FoV)**

Fig. 5 Stereoscopic particle image velocimetry measurement setup.

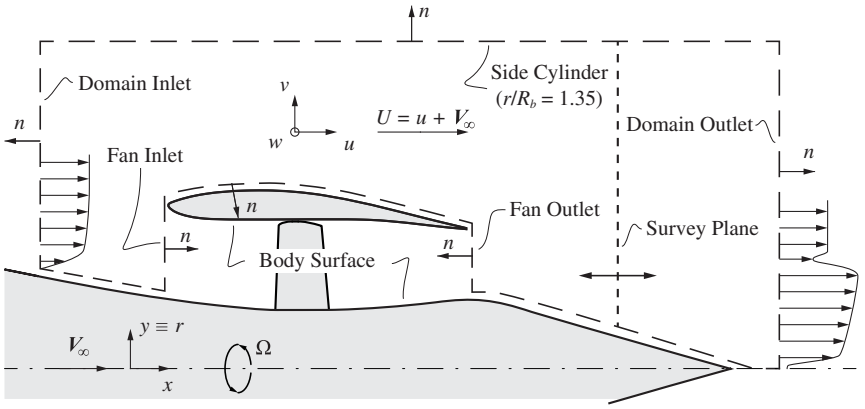

Fig. 6 Control volume and notations defined for the pressure reconstruction and power analysis.

method). The general form of the equation is obtained by deriving the pressure gradient in space:

$$\nabla^2 p = \nabla \cdot \nabla p = \nabla \cdot \left(-\rho \frac{\partial \boldsymbol{V}}{\partial t} - \rho \boldsymbol{V} \cdot \nabla \boldsymbol{V} + \mu \nabla^2 \boldsymbol{V} \right) \tag{1}$$

The particular formulation used in the current study was obtained from this form by making some simplifying assumptions. First, since only phase-uncorrelated PIV data were used, the flow was assumed to be steady ($\partial/\partial t = 0$). Moreover, the flow was assumed incompressible ($\rho = \rho_\infty, \nabla \cdot \boldsymbol{V} = 0$). Lastly, the flow was assumed axisymmetric ($\partial/\partial\theta = 0$). In cylindrical coordinates, $\{x, r, \theta\}$, the following Poisson equation was obtained (derived from Ref. [32]):

$$\begin{aligned} \frac{\partial^2 p}{\partial x^2} + \frac{\partial^2 p}{\partial r^2} = -\rho_\infty \Bigg\{ & \left(\frac{\partial u}{\partial x}\right)^2 + 2\frac{\partial v}{\partial x}\frac{\partial u}{\partial r} + \left(\frac{\partial v}{\partial r}\right)^2 + u\frac{\partial^2 u}{\partial x^2} + v\frac{\partial^2 v}{\partial r^2} \\ & + u\frac{\partial^2 v}{\partial r \partial x} + v\frac{\partial^2 u}{\partial x \partial r} - \frac{\partial}{\partial r}\left(\frac{w^2}{r}\right) \Bigg\} \\ & + \mu_\infty \left\{ \frac{\partial}{\partial x}\nabla^2 u + \frac{\partial}{\partial r}\left(\nabla^2 v - \frac{v}{r^2}\right) \right\} \end{aligned} \tag{2}$$

The equation was solved in the domain using the finite-difference method of Ref. [33]. Spatial derivatives were computed with a three-point central scheme. Dirichlet and Neumann conditions were applied at the domain boundaries. At the boundaries in the isentropic flow region, "Side Cylinder" of Fig. 6, placed at $r/R_b = 1.35$, the static pressure distribution was computed from the velocity by assuming $p_t = p_{t,\infty}$. At all other boundaries, "Domain Inlet," "Domain Outlet," "Fan Inlet," "Fan Outlet," and "Body Surface" of Fig. 6, Neumann conditions were applied. On these boundaries, the static pressure gradient in the boundary-normal direction, n, was obtained from the PIV data. Finally, the total pressure field was calculated from the static pressure and velocity fields using the incompressible Bernoulli's equation.

The inferred pressure field is affected by a stochastic uncertainty originating from the uncertainty of the PIV data that nonlinearly propagates through the numerical process. The uncertainty of the pressure data was estimated by a stochastic Monte Carlo approach, analogously to Ref. [34]. The approach consisted of computing the pressure field from a number of synthetic velocity fields obtained by perturbing the measured PIV data with a pseudo-random uniform error with a magnitude equal to the uncertainty of the PIV data. A converged statistics was reached in 10,000 iterations, and the maximum standard error on the C_{p_t} was equal to 0.06.

2. *Momentum and Power Analysis*

The power analysis of the flowfield followed the definitions and notations of the PBM [4]. Nevertheless, a brief description of the terms and definition used in the analysis is reported here. The power balance equation can be simplified for the current application and presented in a nondimensional form

$$C_{P_k} = C_{\dot{\epsilon}} + C_\phi \tag{3}$$

where C_{P_k}, $C_{\dot{\epsilon}}$, and C_ϕ are, respectively, the nondimensional propulsor mechanical power input, total mechanical power outflow, and viscous dissipation rate. The coefficients were obtained by normalizing with the factor $q_\infty V_\infty S_{\text{ref}}$. Following Ref. [4], $C_{\dot{\epsilon}}$ can be defined as

$$C_{\dot{\epsilon}} = \frac{1}{S_{\text{ref}}} \int_0^\infty \int_0^{2\pi} \left(\frac{U}{V_\infty} C_{p_t} \right) r \, \mathrm{d}\theta \, \mathrm{d}r \tag{4}$$

and decomposed in

$$C_{\dot{\epsilon}} = C_{F_x} + C_{\dot{E}} \tag{5}$$

where C_{F_x} and $C_{\dot{E}}$ are, respectively, the axial momentum flux and kinetic energy deposition rate coefficients. C_{F_x} and $C_{\dot{E}}$ represent the net axial momentum and kinetic energy fluxes across the Survey Plane of Fig. 6.

In particular, the axial momentum flux coefficient C_{F_x}, positive for a thrust excess, was obtained following the approach of Ref. [35]:

$$C_{F_x} = \frac{1}{S_{\text{ref}}} \int_0^\infty \int_0^{2\pi} \left(C_{p_t} + \left(\frac{u}{V_\infty}\right)^2 - \left(\frac{v}{V_\infty}\right)^2 - \left(\frac{w}{V_\infty}\right)^2 \right) r \, \mathrm{d}\theta \, \mathrm{d}r \tag{6}$$

where u, v, and w are the components of the perturbation velocity defined by $(U, V, W) \equiv (u + V_\infty, v, w)$.

The wake blockage effect was taken into account following Ref. [36] for the calculation of the correction ΔC_{F_x}:

$$\Delta C_{F_x} = \frac{1}{S_{\text{ref}}} \frac{u_0}{V_\infty} \int_0^\infty \int_0^{2\pi} \left(\frac{U^*}{V_\infty} - \frac{U}{V_\infty} \right) r \, \mathrm{d}\theta \, \mathrm{d}r \tag{7}$$

where u_0 is the blockage velocity, defined as

$$\frac{u_0}{V_\infty} = \frac{1}{2S_{\text{TS}}} \int_0^\infty \int_0^{2\pi} \left(\frac{U^*}{V_\infty} - \frac{U}{V_\infty} \right) r \, \mathrm{d}\theta \, \mathrm{d}r \tag{8}$$

where S_{TS} is the wind-tunnel test-section cross-sectional area and U^* is defined by

$$\left(\frac{U^*}{V_\infty}\right)^2 = \left(\frac{U}{V_\infty}\right)^2 - C_{p_t} \tag{9}$$

Similarly, $C_{\dot{E}}$ was decomposed as

$$C_{\dot{E}} = C_{\dot{E}_a} + C_{\dot{E}_r} + C_{\dot{E}_t} + C_{\dot{E}_p} \tag{10}$$

where $C_{\dot{E}_a}$, $C_{\dot{E}_r}$, $C_{\dot{E}_t}$, and $C_{\dot{E}_p}$ are, respectively, the axial, radial, and tangential kinetic energy deposition and pressure work rates:

$$C_{\dot{E}_a} = \frac{1}{S_{\text{ref}}} \int_0^{\infty} \int_0^{2\pi} \left(\frac{U}{V_\infty} \frac{\frac{1}{2}u^2}{\frac{1}{2}V_\infty^2} \right) r \, \mathrm{d}\theta \, \mathrm{d}r \tag{11}$$

$$C_{\dot{E}_r} = \frac{1}{S_{\text{ref}}} \int_0^{\infty} \int_0^{2\pi} \left(\frac{U}{V_\infty} \frac{\frac{1}{2}v^2}{\frac{1}{2}V_\infty^2} \right) r \, \mathrm{d}\theta \, \mathrm{d}r \tag{12}$$

$$C_{\dot{E}_t} = \frac{1}{S_{\text{ref}}} \int_0^{\infty} \int_0^{2\pi} \left(\frac{U}{V_\infty} \frac{\frac{1}{2}w^2}{\frac{1}{2}V_\infty^2} \right) r \, \mathrm{d}\theta \, \mathrm{d}r \tag{13}$$

$$C_{\dot{E}_p} = \frac{1}{S_{\text{ref}}} \int_0^{\infty} \int_0^{2\pi} \left(\frac{u}{V_\infty} C_p \right) r \, \mathrm{d}\theta \, \mathrm{d}r \tag{14}$$

Finally, the turbulence kinetic energy flux across the survey plane was computed as

$$C_{\dot{E}_\kappa} = \frac{1}{S_{\text{ref}}} \int_0^{\infty} \int_0^{2\pi} \left(\frac{U}{V_\infty} \frac{\kappa}{V_\infty^2} \right) r \, \mathrm{d}\theta \, \mathrm{d}r \tag{15}$$

where κ is the turbulence kinetic energy; κ is computed from the PIV measurements as

$$\kappa = \frac{1}{2}\left(\sigma_u^2 + \sigma_v^2 + \sigma_w^2\right) \tag{16}$$

where σ_u, σ_v, and σ_w are the standard deviations of the velocity components. Any unsteady component of the flowfield also contributes to the estimation of the standard deviation and hence to the turbulence kinetic energy.

III. Results

The aerodynamic performance of the PFC configuration is the result of the complex interaction between the fuselage airframe and the aft-fuselage mounted fan. The pressure and velocity field induced by the fan affects the flowfield downstream and upstream of the fan itself. To capture the aerodynamic response of the overall configuration and the subsystem interactions, different measurement techniques were used with different objectives. Balance measurements were used to quantify the overall system performance that, in the analyzed cases, are characterized by the net axial force acting on the fuselage–fan assembly. Total pressure and PIV measurements assessed the 3-D time-averaged flowfield in the wake and around the BLI propulsor. These flowfield data served to quantify the momentum and power distribution around the fan and in the near wake.

A. Configuration Performance

Balance measurements were performed for a range of fan operating conditions, defined by the fan tip speed ratio U_{tip}/V_∞. At each fan speed setting, the net axial force being exerted on the fuselage–fan assembly was measured. As already explained in Sec. II.B.1, the net axial force of the fuselage–fan assembly was a direct output of the external balance. The net axial force coefficient is defined as $C_N = N/(q_\infty S_{\text{ref}})$, with the axial force N positive for an excess of thrust. The drag coefficient of the BF configuration, C_{D_0}, is used as reference. The ratio C_N/C_{D_0} is a measure of the net momentum excess due to the powered configuration with respect to the momentum deficit of the baseline fuselage configuration. To achieve measurements in the desired range of C_N/C_{D_0}, the freestream velocity was changed in combination with the fan shaft speed, leading to a variation of the fuselage length-based Reynolds number Re_{L_b} between 3.5×10^6 and 4.7×10^6. To minimize the effects of the changing Reynolds number, the drag coefficient of the BF was also assessed at the same freestream velocities and used to obtain the non-dimensional fraction.

Figure 7 shows the fuselage–fan net axial force coefficient against the fan tip speed ratio for different freestream velocities. The plot of

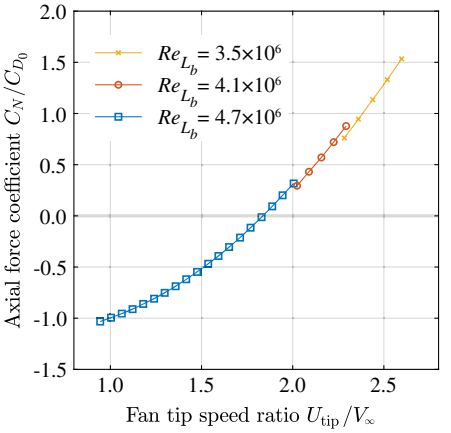

Fig. 7 Net axial force coefficient for different fuselage–fan operating conditions. External balance measurements taken at different freestream velocities V_∞.

Fig. 7 shows that C_N non-linearly increased with increasing U_{tip}/V_∞. At around $U_{\text{tip}}/V_\infty = 1$, the fuselage–fan assembly produced a net force equal to that of the bare-fuselage drag resulting in $C_N/C_{D_0} = -1$. Therefore, at this condition, the net effect of the fan installation on the measured axial force was zero. The axial equilibrium condition ($C_N = 0$) was reached for $U_{\text{tip}}/V_\infty = 1.84$. For higher tip speed ratios, the net force became positive, meaning a thrust excess. The curves were measured at three different freestream velocities and Reynolds numbers and do not fall perfectly on each other, although being expressed in nondimensional parameters. This is due to the effect of the Reynolds number on the airframe and fan force coefficients. In particular, an increase in the Reynolds number resulted in an upward shift of the curve, in agreement with what found in Ref. [37]. The net axial force is the integral of the pressure and shear stresses on the fuselage and propulsor surfaces. In general, the integral over the fuselage and shroud surfaces gives a negative contribution to C_N, whereas the integral over the fan blades gives a positive contribution. At a fixed U_{tip}/V_∞, increasing the Reynolds number produces, in absolute values, a reduction of the airframe contribution and an increase of the fan contribution. Dividing C_N by C_{D_0}, as in the plot of Fig. 7, partially compensates this Reynolds number effect because it accounts for the change of the airframe contribution. On the other hand, the effect that the Reynolds number had on the fan contribution is not compensated, resulting in the upward shift of the curves in the plot of Fig. 7.

B. Flowfield Analysis in Axial Equilibrium Conditions

1. *Wake Flowfield*

Velocity and total pressure measurements were carried out in the WP-FoV plane as described in Secs. II.B.2 and II.B.3. Figure 8 shows the distributions of the total pressure and of the axial, transverse (sum of the tangential and radial components), and turbulence kinetic energy flux densities in the wake. Data are shown for the BF case (left subplots of Fig. 8) and the PF cases (central subplots of Fig. 8). In addition, the difference between the BF and the powered case is shown in the right subplots of Fig. 8. Because the fan was equipped with outlet vanes (see Fig. 4d), the wakes of the vanes were clearly visible even in the phase-averaged field. Because of the swirl in the propulsor slipstream, the azimuthal position of the outlet vanes wakes was a function of the axial distance between the outlet plane and the survey plane. To have a consistent comparison of the powered and unpowered cases, the fan slipstream was azimuthally averaged.

Figure 8a (left) shows that the total pressure distribution in the wake of the BF configuration deviated from being axisymmetric because of the junction flow generating at the fuselage-fairings intersection. The interaction of the fairing pressure field and the upstream fuselage boundary layer created a pair of horseshoe vortex structures, symmetric around both the xz and xy planes. These vortices entrained high-momentum flow inside the fuselage boundary layer, producing the C_{p_t}

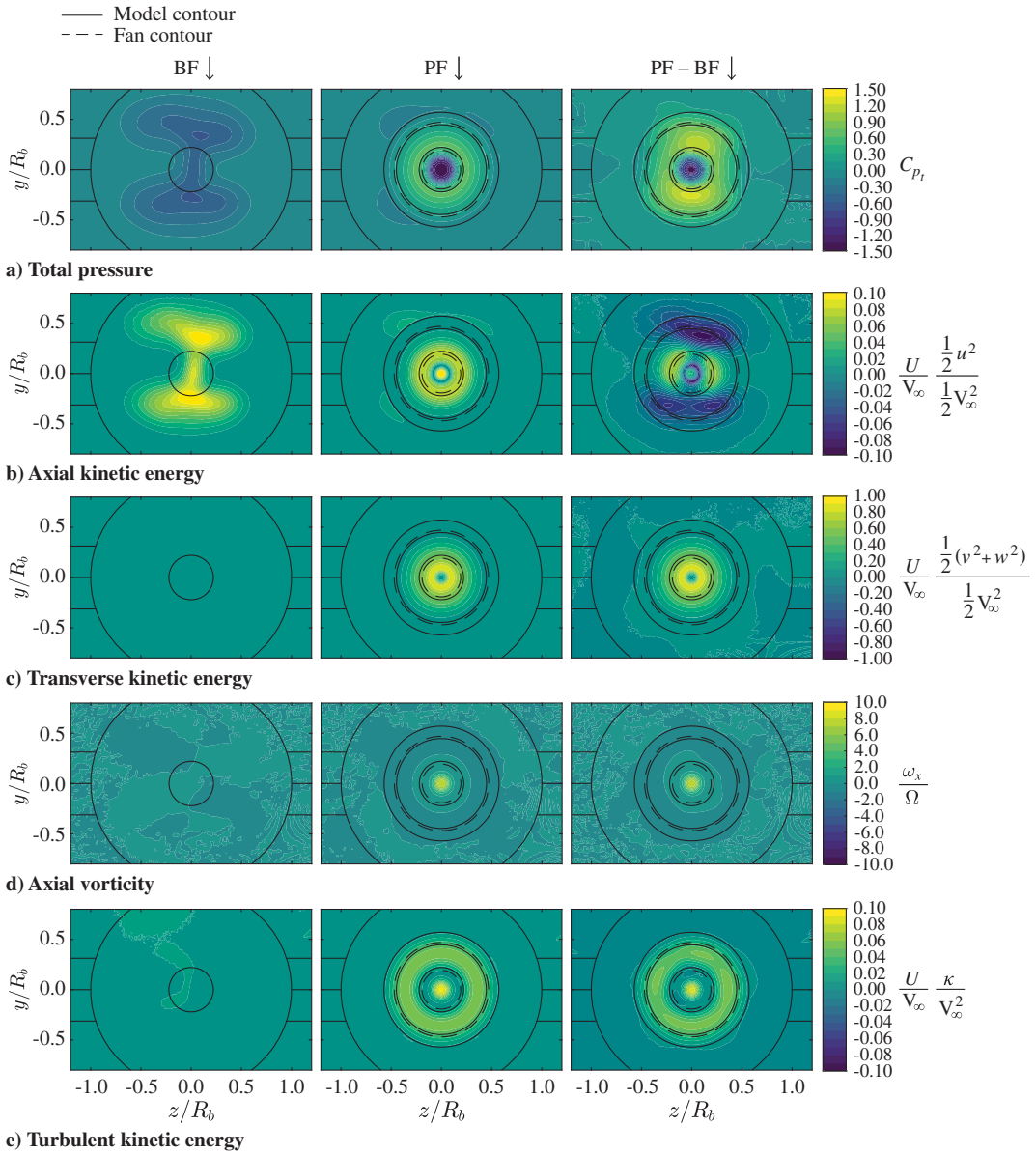

Fig. 8 Momentum and power decomposition in the WP-FoV plane for the bare fuselage case (BF), powered fuselage case at $C_N = 0$ (PF), and their difference (PF−BF). Total pressure and PIV measurements at $Re_{L_b} = 4.7 \times 10^6$.

pattern reported in the left subplot of Fig. 8a. The effect of the fuselage–fairing junction flow is also recognizable in the axial kinetic energy distribution shown in Fig. 8b (left). In the wake of the BF, the axial kinetic energy flux reached the highest values in the flow regions of low total pressure. The transverse and turbulence kinetic energy distributions, shown in left subplots of Figs. 8c and 8e, respectively, are instead relatively low in the BF case.

In the PF case, the total pressure distribution (central subplot of Fig. 8a) was equal or higher than the freestream value in the fan slipstream. This was due to the momentum increase introduced by the fan. However, a very low total pressure value was found close to the axis, due to the onset of rotational flow around the fan hub. In fact, as Fig. 8d (center) shows, high axial vorticity was found in the PF case in proximity of the axis. This vortical flow also resulted in a large transverse kinetic energy (Fig. 8c). Because of the conservation of angular momentum, when a fluid particle moves toward the fuselage axis, its angular velocity linearly increases to keep the angular momentum constant. To compensate for the increasing centrifugal force, the centripetal pressure force, proportional to the pressure gradient in the radial direction, increases with the square of the angular velocity. As a consequence, the static pressure and the axial velocity significantly decreased toward the fuselage axis. Moreover, the associated velocity gradient enhanced the viscous losses and the viscous core of the vortical structure is clearly identifiable from Fig. 8c (center), where the transverse energy linearly decreased to zero from $r/R_b = 0.1$ toward the axis. The turbulence kinetic energy was also substantially increased by the fan in the powered conditions, as shown in Fig. 8e. In particular, the highest turbulence intensities were measured close to the axis, in coincidence of the vortical structure described above. The ensemble-average flowfields shown for the powered cases are obtained by averaging out phase-free instantaneous PIV images. Therefore, the unsteadiness of the flowfield, due to the fan blades slipstream, contributed to the standard deviation of the instantaneous velocity fields and hence affected the estimation of the turbulence statistics.

2. *Symmetry Plane Flowfield*

To visualize the flowfield around the propulsor and quantify the development of the fuselage boundary layer across the fan plane, the velocity field was measured in the horizontal symmetry plane of the model (SP-FoV PIV setup of Sec. II.B). Figure 9 shows the mean and turbulent flowfields around the fuselage aft-cone section for the BF case and the PF case in axial equilibrium condition. Phase-uncorrelated PIV measurements were taken at a freestream

velocity of 20 m/s, and for the powered configuration without outlet vanes mounted. Therefore, a direct quantitative comparison with Fig. 8 is impossible because of the flowfield induced by the outlet vanes.

Streamlines projections for both the BF and PF cases are shown in Fig. 9a. Because the flow is 3-D, these do not coincide with the actual streamlines in the flow regions where swirl component was not zero. Comparing the two cases, it is possible to appreciate the key effects of the fuselage–fan on the surrounding flow. First, upstream of the fan, the boundary-layer flow is directed inboard, because of the locally increased mass flow rate due to the fan suction. Second, downstream of the fan, the boundary layer contracts as a consequence of the fan slipstream contraction. Further downstream, due to the onset of the vortical flow structure already described in Sec. III.B.1, the fan slipstream is displaced outboard before leaving the fuselage trailing edge.

Figure 9b shows the total pressure coefficient for the BF case (left subplot) and the PF case (right subplot). The total pressure field was inferred from the PIV measurements via the method discussed in Sec. II.D.1. The turbulent boundary-layer flow around the BF is clearly visible and characterized by a total pressure value lower than the freestream. The boundary-layer physical thickness, δ_{99}, defined as the radial position at which $p_t/p_{t\infty} = 0.99$, was estimated at $y/R_b = 0.67$ at the fan location ($x/L = 0.94$) for the BF case. The total pressure distribution for the PF case for $C_N = 0$ is shown in Fig. 9b (right). The contour shows that the fuselage boundary layer is larger than the fan, and approximately 30% of δ_{99} is not ingested by the propulsor. Downstream of the fan, the total pressure is higher than the freestream value due to the momentum addition of the fan. In addition, the edge of the fuselage boundary layer is thinner than in the BF case and contracts more toward the fuselage trailing edge as a consequence of the local negative axial pressure gradient and slipstream contraction (see again Fig. 9a). At the shroud trailing edge, the viscous boundary layer over the shroud external surface mixed with the fan slipstream, creating a relatively sharp mixing layer with strong total pressure and velocity gradients.

Figure 9c shows the axial disturbance velocity component, $u = U - V_\infty$, for the BF case (left subplot) and the PF cases (right subplot). The effect of the BLI fan propagates upstream of the shroud, where the boundary-layer flow is accelerated when compared with the unpowered case. Obviously, the slipstream of the fan also shows an increased velocity due to the imposed momentum increase. Moreover, the interaction between the shroud and the fuselage outer boundary-layer flow is clearly visible. The stagnation points at the leading and trailing edges of the shroud, as well as the suction and compression around the shroud contour can be seen (see right subplots of Figs. 9a and 9c).

The out-of-plane velocity component is shown in Fig. 9d. The distribution of w across the shroud exit is non-uniform, and follows the blade loading distribution with the highest values found around the fan tip (see right subplot of Fig. 9d). As we move downstream toward the fuselage trailing edge, higher out-of-plane velocities are found, due to the slipstream contraction and the conservation of angular momentum. In addition, a strong increase of tangential velocity was measured at the trailing edge of the fuselage due to the onset of a vortex, as discussed in Sec. III.B.1. In the PF case

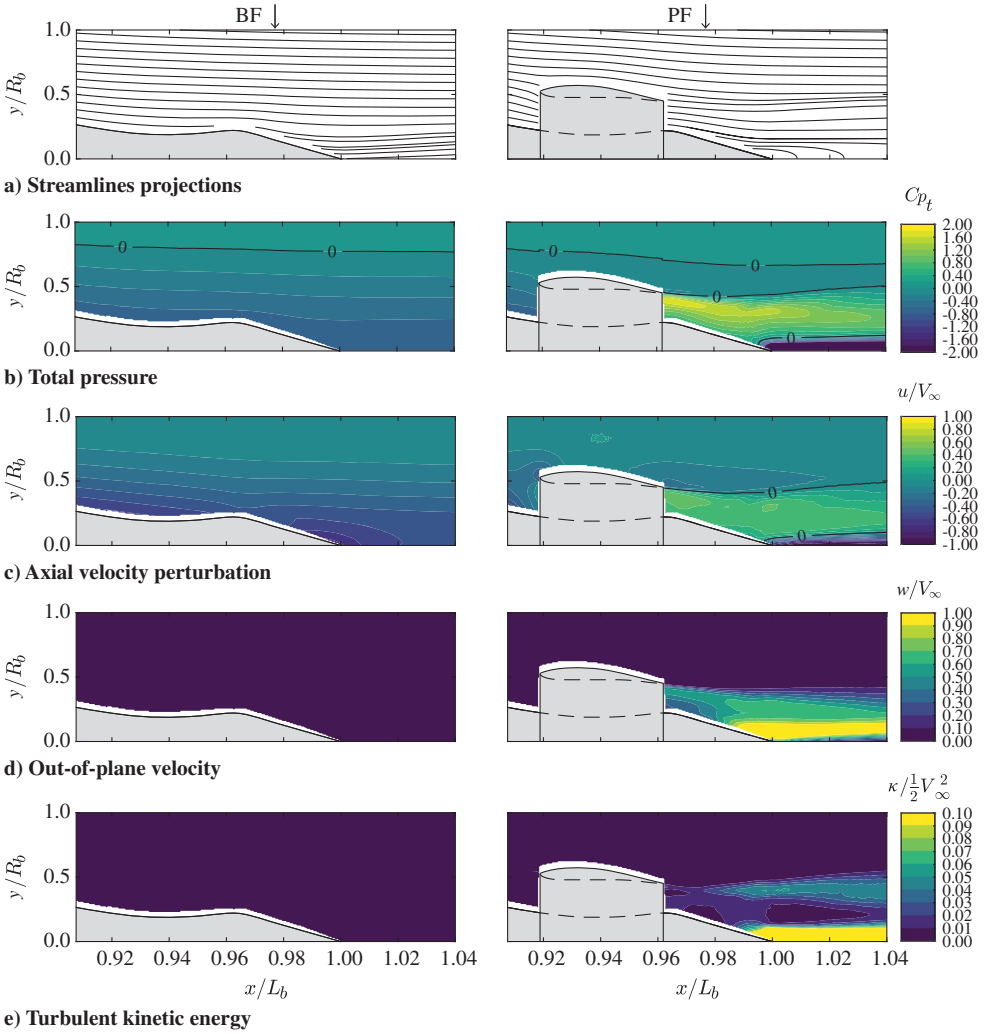

Fig. 9 Flowfield around the fuselage-mounted propulsor. BF case (left) and PF case (right). PIV measurements in the SP-FoV plane at $V_\infty = 20$ m/s. PF case at $C_N = 0$ and without the outlet vanes.

(right subplots of Fig. 9), this vortex structure was enhanced by the fact that the trailing edge of the fuselage was spinning together with the fan and hence introducing angular momentum in the flow. Moreover, the outlet vanes did not influence significantly the vortex structure. This can be confirmed by comparing qualitatively Figs. 8a (center) and 9b (right), which show the total pressure distribution for the PF case with and without outlet vanes, respectively. In both cases, a total pressure deficit of similar strength and extension was found around the fuselage axis. This could be because the outlet vanes did not significantly alter the swirl distribution due to their design.

The hub vortex structure also features a relatively high turbulence level, as testified by Fig. 9e (right). Turbulence kinetic energy was also measured in the shear layer between the fan slipstream and the outer fuselage boundary layer.

To analyze the effect of the BLI fan on the local boundary-layer flow, boundary-layer profiles are shown for the BF and the PF at $C_N = 0$ in Fig. 10. The location of the survey stations is sketched in Fig. 10a, whereas Fig. 10b shows the streamlines projections upstream and downstream of the shroud. The plots of Fig. 10c confirm that the upstream effect of the BLI fan on the total pressure distribution is weak. However, a strong effect is found on the velocity field, due to the pressure field imposed by the fan. This results in an increased wall-tangential velocity u_t in the inboard region of the boundary layer and in the onset of a negative (i.e., inboard) normal velocity component u_n. Downstream of the propulsor, the effect of the BLI propulsor to the local flow is much stronger, as shown in Fig. 10d. In particular, two key effects can be understood from the C_{p_t} profile: first, the high-momentum flow ($C_{p_t} > 0$) carried by the fan slipstream entrains the boundary layer, increasing the total pressure also outside the fan slipstream itself compared with the BF case. Second, the boundary layer in the PF case becomes thinner than the BF case, due to the local slipstream contraction. In particular, at station B, the physical boundary-layer thickness δ_{99} decreases from $0.67R_b$ for the BF case to $0.56R_b$ for the PF case, resulting in a 15% thinner boundary layer.

3. *Power Balance Across the BLI Propulsor*

The PBM was applied to these flowfields in order to quantitatively assess the integral momentum and power fluxes (or deposition rates) across the propulsor location. The control volume and notations defined in Fig. 6 of Sec. II.D were used for the integral analysis of the flowfield. The momentum and power fluxes were computed on a survey plane perpendicular to the freestream velocity direction moving from the domain inlet to the domain outlet along the axial direction x (see Fig. 6).

Figure 11 shows the variation of the integral momentum and power deposition rates along the fuselage axis for the BF and the PF cases in axial equilibrium. For the PF case, the integral values are discontinuous across the shroud location as the velocity and pressure data inside the shroud are missing. Figure 11a shows the axial momentum flux coefficient C_{F_x} as a function of the axial position x/L_b, as defined by Eq. (6) in Sec. II.D.2. C_{F_x} represents the amount of axial momentum

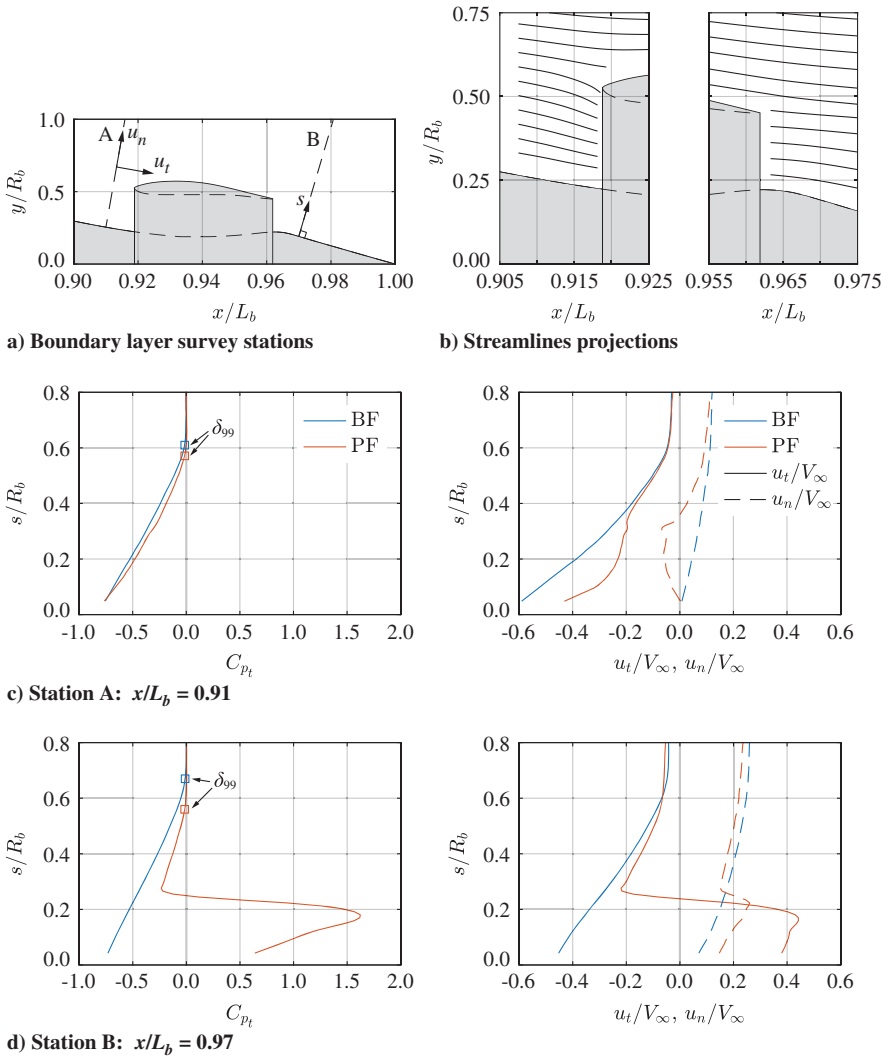

a) Boundary layer survey stations **b) Streamlines projections**

c) Station A: $x/L_b = 0.91$

d) Station B: $x/L_b = 0.97$

Fig. 10 Boundary-layer profiles for the BF and PF cases. PIV measurements in the SP-FoV plane at $V_\infty = 20$ m/s. PF case at $C_N = 0$ and without the outlet vanes.

deficit (or excess) in the flow at the specific axial position, and it is linked to the configuration drag (or thrust). For the BF case, C_{F_x} is always negative and is monotonically increasing in absolute value due to the viscous dissipation taking place in the fuselage boundary layer. Interestingly, C_{F_x} showed a relatively quick change in slope as we move toward the trailing edge ($x/L_b = 1$) and kept decreasing at the same rate in the near wake ($x/L_b > 1$) up to the end of the field of view. For the PF case, the momentum deficit upstream the shroud was increased by around 10% with respect to the BF case due to the detrimental interaction effects of the operating shrouded fan. Across the propulsor, the momentum flux showed a step change due to the addition of momentum in the flow by the fan. In this measured case, even though the balance measured a zero axial force, the thrust provided by the fan exceeded the fuselage momentum deficit, resulting in a momentum excess in the fan slipstream.

Figure 11b shows the variation along the axis of the total mechanical energy flux $C_{\dot{\varepsilon}}$ and the kinetic energy deposition rate $C_{\dot{E}}$, obtained as the difference between $C_{\dot{\varepsilon}}$ and C_{F_x} (see Eqs. (4–10) of Sec. II.D.2). $C_{\dot{\varepsilon}}$ and $C_{\dot{E}}$ varied along the fuselage axis similarly to C_{F_x} both for the BF and PF cases. For the BF case, $C_{\dot{\varepsilon}}$ monotonically decreased when moving downstream, driven by C_{F_x} (see Eq. (5)). On the other hand, $C_{\dot{E}}$ increases with x, growing from approximately 0.016 upstream the fan, to 0.019 at the fuselage trailing edge and to 0.020 at $x/L_b = 1.05$. The power balance of the BF can be obtained by simplifying Eq. (3) to $-C_{F_x} = C_{\dot{E}} + C_{\phi}$. At the trailing edge of the fuselage ($x/L_b = 1$), $C_{\dot{E}}/-C_{F_x} = 0.13$, which means that approximately 13% of the total power losses occurs in the wake of the fuselage. This value also represents the ideal power benefit of BLI for the fuselage model, achievable with an ideal BLI propulsor that entirely recovers the energy deficit in the fuselage boundary layer. Note that this benefit refers to the power needed to propel the fuselage only and needs to be scaled to the whole aircraft level if required. The value of $C_{\dot{E}}$ for the powered configuration upstream the fan was higher than for the BF case, due to the suction that the fan imposed to the upstream boundary-layer fluid. Across the shrouded fan, the mechanical power flux coefficient $C_{\dot{\varepsilon}}$ experienced a jump, which is linked to the mechanical power transmitted by the fan into the fluid. $C_{\dot{\varepsilon}}$ shows a slight increase immediately downstream of the shroud exit. This is thought to be due to the influence of the spinning nozzle plug, which introduced tangential momentum in the flow. This resulted in an increase of $C_{\dot{\varepsilon}}$ without adding to the axial momentum flux. This is corroborated by Fig. 12c. Also $C_{\dot{E}}$ showed a jump across the fan and approximately 23% of the total mechanical power introduced by the BLI fan accounted for the $C_{\dot{E}}$ component and subsequently dissipated in the wake.

$C_{\dot{E}}$ is the sum of the four different terms defined in Eqs. (11–14) which are the power fluxes associated with the three velocity components and the static pressure work. Figure 12 shows how each individual term varied along the fuselage axis for both the BF case and PF in axial equilibrium case. The discontinuity in the curves for the PF cases is due to the missing flowfield data inside the shroud. By comparing the curves upstream the shroud leading edge for the two cases, it can be seen that the effect of the BLI fan was to accelerate the incoming flow, producing a decrease in modulus of both $C_{\dot{E}_a}$ and $C_{\dot{E}_p}$ (Figs. 12a and 12d). At the same time, an increase of $C_{\dot{E}_r}$ (Fig. 12b) was measured, due to the induced radial flow component already discussed (see Fig. 10c). Downstream the shroud outlet, the tangential kinetic energy flux $C_{\dot{E}_t}$ (Fig. 12c) strongly increased in the powered case as a consequence of the tangential momentum introduced by the fan blades becoming the dominant component of $C_{\dot{E}}$. In a more realistic case at full-flight scale, this component could be effectively minimized through an optimized stator stage.

C. Effect of Fan-Thrust-to-Body-Drag Ratio

The previous subsection has covered the performance analysis of the PFC in cruise conditions, for which the net axial force acting on the fuselage–fan assembly was zero. To assess the effect of varying thrust settings on the aerodynamics of the overall configuration, measurements were taken at different net axial force coefficients. PIV measurements were used to quantify the boundary-layer and near-wake flowfields around the propulsor and to infer the total pressure distribution, with the method discussed in Sec. II.D.1. The axial velocity and total pressure profiles at the fan inlet ($x/L_b = 0.91$), fan outlet ($x/L_b = 0.97$), and in the fuselage near wake ($x/L_b = 1.06$) for different net axial force coefficients are shown in Fig. 13. A number of fan operating conditions were assessed for which $-1.0 \leq C_N/C_{D_0} \leq 1.0$.

The effect of the fan on the upstream flow is clearly visible in Figs. 13a (left) and 13b (left). Increasing the axial force produced a visible suction effect on the boundary layer, resulting in a higher velocity in the lower part of the profile (left subplot of Fig. 13a). Contrarily, the effect on the upstream total pressure profile is not significant (left subplot of Fig. 13b). This entails that the upstream effect of the BLI fan was comparable to that of an inviscid (potential) actuator disk, and the viscous interaction with the incoming boundary layer is of second order. Note that for $C_N/C_{D_0} = -1$ the fan was actually slowing down the incoming boundary layer even at a constant total pressure value. This was probably because the shroud was operating at an off-design condition, and hence spillage occurred as the mass flow required by the fan was lower than the design one.

Downstream the fan outlet (central subplots of Figs. 13a and 13b), the slipstream of the fan is clearly recognizable in the powered cases as the axial velocity and total pressure are both higher than in the BF case. In particular, for the $C_N/C_{D_0} = -1$ case the total pressure profile shows a slightly increased total pressure over the BF case that compensates for the shroud viscous wake, centered at around $r/R_b = 0.45$, producing a zero axial force overall.

Figures 13a (right) and 13b (right) show the velocity and total pressure distributions in the model wake. C_{p_t} shows a very low value at the axis for the powered cases due to the hub vortex formation described in Sec. III.B, which increased in strength for increasing C_N. Moreover, at $C_N/C_{D_0} = -0.5$ both the average U/V_∞ and C_{p_t} were closer to the freestream values (respectively, 1 and 0). This entails that

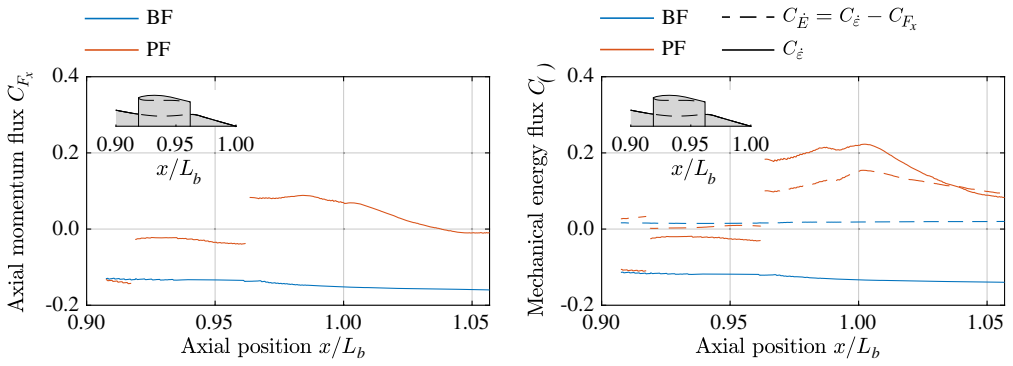

a) Axial momentum flux **b) Mechanical energy flux**

Fig. 11 Variation along the axial direction of the integral momentum and mechanical energy fluxes across the fuselage aft section. PF case taken for $C_N = 0$.

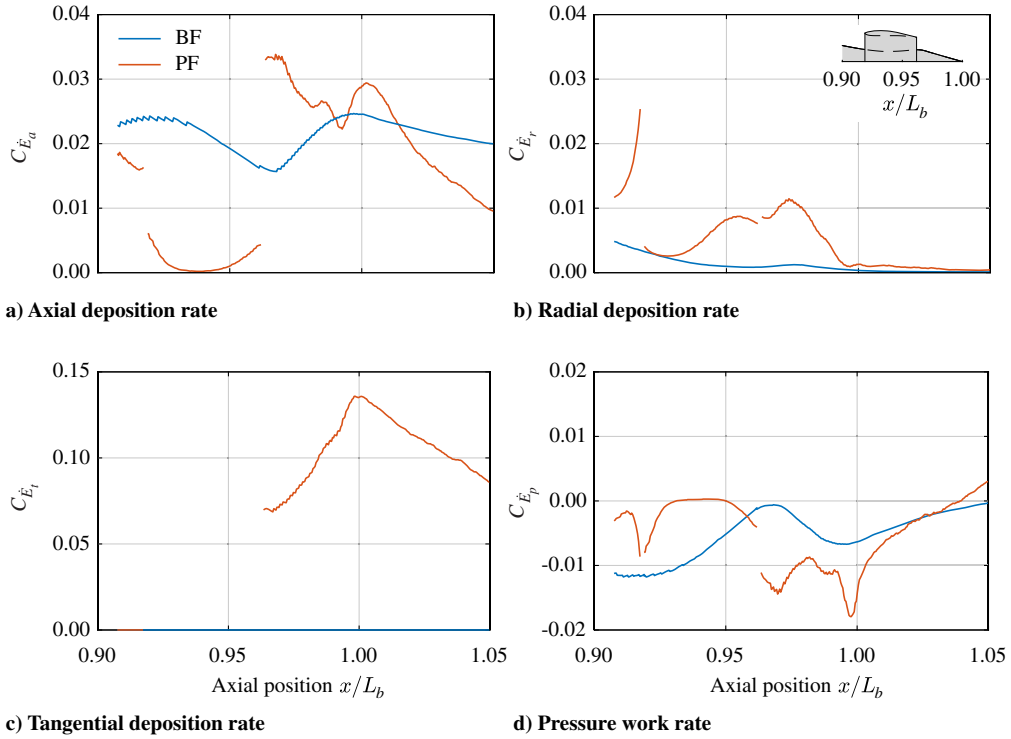

a) Axial deposition rate **b) Radial deposition rate**

c) Tangential deposition rate **d) Pressure work rate**

Fig. 12 Integral mechanical energy flux components across the fuselage aft section. Powered measurements taken in axial equilibrium conditions ($C_N/C_{D_0} = 0$).

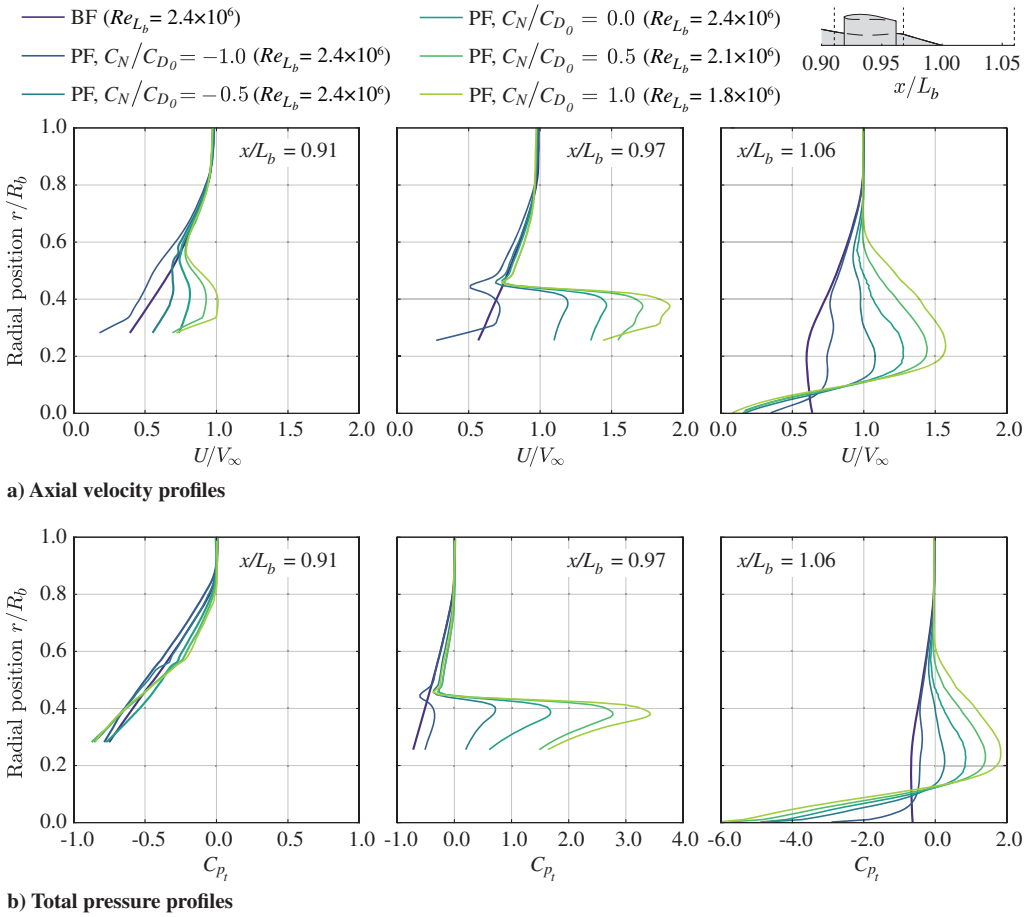

a) Axial velocity profiles

b) Total pressure profiles

Fig. 13 Axial velocity and total pressure profiles for different net axial force conditions. Velocity and pressure data from the SP-FoV PIV setup.

$C_N/C_{D_0} = -0.5$ was the condition, among the measured ones, for which the benefit of BLI could be maximum. This can be explained by the fact that only a part of the boundary layer was ingested by the BLI propulsor. As a consequence, only part of the momentum and kinetic energy in the boundary layer were ingested. Therefore, to compensate for the ingested deficit, the thrust produced was lower than the fuselage drag. For higher thrust conditions (i.e., for $C_N/C_{D_0} > -0.5$), a residual momentum flux was measured in the fan slipstream (right subplot of Fig. 13b). This means that the momentum and energy introduced by the fan into the boundary layer exceeded the ingested deficit, potentially reducing the advantage of BLI.

To understand the effect of the fan-thrust-to-body-drag ratio on the wake losses, the mechanical power flux $C_{\dot{\varepsilon}}$ and its two contributions C_{F_x} and $C_{\dot{E}}$ were computed in the near wake of the model. Figure 14 presents the three terms for the BF and PF cases for different C_N/C_{D_0} values at $x/L_b = 1.05$. The plot shows that for the BF $C_{\dot{E}}$ was approximately equal, in modulus, to 13% of C_{F_x}, as already pointed out in Sec. III.B. Similar values were found for the powered case for $C_N/C_{D_0} = -1.0$, as expected. Increasing the thrust setting leads to a continuous increase of the power flux in the wake. Interestingly, even though the momentum deficit was the closest to zero for $C_N/C_{D_0} = 1.0$, $C_{\dot{E}}$ was largely increased with respect to the BF, meaning that a substantial part of the energy introduced in the flowfield was still dissipated in the wake of the model. The case for $C_N/C_{D_0} = -0.5$ shows the minimum value of $C_{\dot{E}}$, suggesting that this is the condition for which the BLI benefit is maximum. However, in a more realistic configuration, where the swirl in the fan slipstream is mostly recovered, a lower $C_{\dot{E}_t}$ would be measured. As a consequence, the minimum $C_{\dot{E}}$ would be probably found at a higher C_N/C_{D_0} ratio. At larger axial forces both C_{F_x} and $C_{\dot{E}}$ increased, but at different rates. This suggests that, relatively to the total power flux $C_{\dot{\varepsilon}}$, at higher thrust settings, a smaller share of the wake energy was dissipated in the wake, whereas a larger share of energy was instead related to the momentum excess.

IV. Conclusions

This paper presented the results of a low-speed wind-tunnel test of a Propulsive Fuselage Concept (PFC). This work represents the first experimental aerodynamic investigation concerning fuselage-BLI. The experimental setup consisted of an axisymmetric fuselage with an embedded boundary-layer-ingesting propulsor. The flowfield around the BLI fan was quantified with PIV measurements and used to perform a power and momentum analysis of the configuration through the PBM.

Results have shown the following:

1) The BLI propulsor strongly affects the surrounding flowfield, modifying the fuselage boundary-layer flow both upstream and downstream of the propulsor location. The key effects of the BLI fan on the fuselage boundary layer are as follows: i) upstream of the propulsor, an increased mass flow flux in the inboard region of the boundary layer, due to the fan suction effect; ii) downstream of the propulsor, the boundary layer is thinner than in the BF case, due to the slipstream contraction; iii) at the fuselage trailing edge, a strong hub vortex is induced by the swirl component, resulting in a region of very low total pressure, which increases the drag and penalizes the performance.

2) Through the application of the PBM, the distribution of momentum and mechanical energy in the boundary-layer flow was quantified. For the axial equilibrium conditions, where $C_N/C_{D_0} = 0$, the effect of the fan is to increase in absolute value the axial momentum flux in the upstream boundary layer with respect to the BF. At the same time, the kinetic energy deposition rate is increased upstream of the fan, due to the suction imposed by the fan on the fuselage boundary layer.

3) The effect of varying the fan thrust setting on the aerodynamic performance was quantified through the PBM. The analysis showed that performance quickly diverges from the ideal wake-filling conditions when increasing the thrust setting. In fact, it was found that the mechanical energy dissipated in the downstream wake increases more than linearly with the net axial force coefficient C_N. Moreover, a larger share of the total mechanical energy is associated with the momentum addition of the BLI fan.

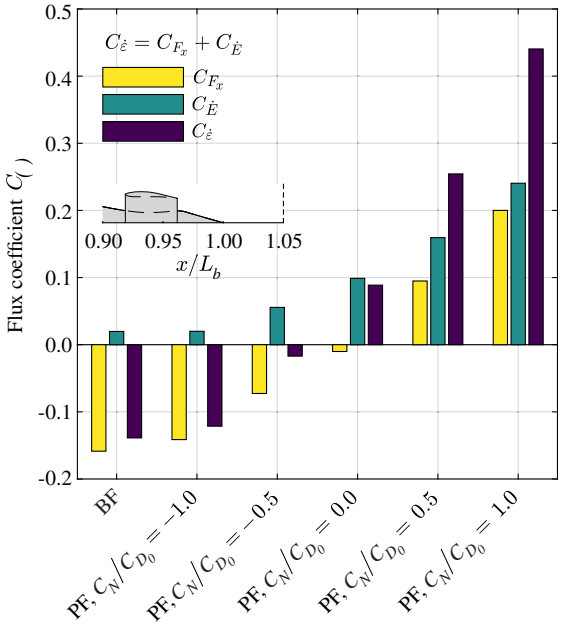

Fig. 14 Power flux components in the near wake of the body ($x/L_b = 1.05$) for different fan settings.

Acknowledgments

This work was conducted within the CENTRELINE project, which has received funding from the European Union's Horizon 2020 research and innovation program under Grant Agreement No. 723242. The authors would like to thank Tomas Sinnige, Daniele Ragni, Reynard de Vries, Nando van Arnhem, and Sumit Tambe for their support.

References

[1] Betz, A., *Introduction to the Theory of Flow Machines*, Pergamon, Oxford, 1966, pp. 215–220, Chap. 59. https://doi.org/10.1016/C2013-0-05426-6

[2] Smith, L. H., "Wake Ingestion Propulsion Benefit," *Journal of Propulsion and Power*, Vol. 9, No. 1, 1993, pp. 74–82. https://doi.org/10.2514/3.11487

[3] Habermann, A. L., Bijewitz, J., Seitz, A., and Hornung, M., "Performance Bookkeeping for Aircraft Configurations with Fuselage Wake-Filling Propulsion Integration," *CEAS Aeronautical Journal*, Vol. 11, No. 2, 2020, pp. 529–551. https://doi.org/10.1007/s13272-019-00434-w

[4] Drela, M., "Power Balance in Aerodynamic Flows," *AIAA Journal*, Vol. 47, No. 7, 2009, pp. 1761–1771. https://doi.org/10.2514/1.42409

[5] Lv, P., Gangoli Rao, A., Ragni, D., and Veldhuis, L., "Performance Analysis of Wake and Boundary-Layer Ingestion for Aircraft Design," *Journal of Aircraft*, Vol. 53, No. 5, 2016, pp. 1517–1526. https://doi.org/10.2514/1.C033395

[6] Hall, D. K., Huang, A. C., Uranga, A., Greitzer, E. M., Drela, M., and Sato, S., "Boundary Layer Ingestion Propulsion Benefit for Transport Aircraft," *Journal of Propulsion and Power*, Vol. 33, No. 5, 2017, pp. 1118–1129. https://doi.org/10.2514/1.B36321

[7] Lv, P., Ragni, D., Hartuc, T., Veldhuis, L., and Gangoli Rao, A., "Experimental Investigation of the Flow Mechanisms Associated with a Wake-Ingesting Propulsor," *AIAA Journal*, Vol. 55, No. 4, 2017, pp. 1332–1342. https://doi.org/10.2514/1.J055292

[8] Drela, M., "Development of the D8 Transport Configuration," *29th AIAA Applied Aerodynamics Conference*, AIAA Paper 2011-3970, 2011. https://doi.org/10.2514/6.2011-3970

[9] Uranga, A., Drela, M., Greitzer, E. M., Hall, D. K., Titchener, N. A., Lieu, M. K., Siu, N. M., Casses, C., Huang, A. C., Gatlin, G. M., and Hannon, J. A., "Boundary Layer Ingestion Benefit of the D8 Transport Aircraft," *AIAA Journal*, Vol. 55, No. 11, 2017, pp. 3693–3708. https://doi.org/10.2514/1.J055755

[10] Wiart, L., Atinault, O., Boniface, J.-C., and Barrier, R., "Aeropropulsive Performance Analysis of the NOVA Configurations," *30th Congress of the International Council of the Aeronautical Sciences*, ICAS Paper 2016-0092, 2016.

[11] Hall, C. A., Schwartz, E., and Hileman, J. I., "Assessment of Technologies for the Silent Aircraft Initiative," *Journal of Propulsion and Power*, Vol. 25, No. 6, 2009, pp. 1153–1162. https://doi.org/10.2514/1.43079

[12] Steiner, H.-J., Seitz, A., Wieczorek, K., Plötner, K., Isikveren, A. T., and Hornung, M., "Multi-Disciplinary Design and Feasibility Study of Distributed Propulsion Systems," *28th International Congress of the Aeronautical Sciences*, ICAS Paper 2012-1.7.5, 2012.

[13] Castillo Pardo, A., and Hall, C., "Aerodynamics of Boundary Layer Ingesting Fuselage Fans," *24th ISABE Conference*, 2019. https://doi.org/10.1115/1.4049918

[14] Isikveren, A. T., Seitz, A., Bijewitz, J., Mirzoyan, A., Isyanov, A., Grenon, R., Atinault, O., Godard, J.-L., and Sütckl, S., "Distributed Propulsion and Ultra-High By-Pass Rotor Study at Aircraft Level," *Aeronautical Journal*, Vol. 119, No. 1221, 2015, pp. 1327–1376. https://doi.org/10.1017/S0001924000011295

[15] Seitz, A., Habermann, A. L., Peter, F., Troeltsch, F., Castillo Pardo, A., Della Corte, B., van Sluis, M., Goraj, Z., Kowalski, M., Zhao, X., Gronstedt, T., Bijewitz, J., and Wortmann, G., "Proof of Concept Study for Fuselage Boundary Layer Ingesting Propulsion," *Aerospace*, Vol. 8, No. 1, 2021, p. 16. https://doi.org/10.3390/aerospace8010016

[16] Seitz, A., Habermann, A. L., and van Sluis, M., "Optimality Considerations for Propulsive Fuselage Power Savings," *Proceedings of the Institution of Mechanical Engineers, Part G: Journal of Aerospace Engineering*, Vol. 235, No. 1, 2021, pp. 22–39. https://doi.org/10.1177/0954410020916319

[17] Welstead, J., and Felder, J. L., "Conceptual Design of a Single-Aisle Turboelectric Commercial Transport with Fuselage Boundary Layer Ingestion," *54th AIAA Aerospace Sciences Meeting*, AIAA Paper 2016-1027, 2016. https://doi.org/10.2514/6.2016-1027

[18] Kenway, G. K., and Kiris, C. C., "Aerodynamic Shape Optimization of the STARC-ABL Concept for Minimal Inlet Distortion," *AIAA/ASCE/AHS/ASC Structures, Structural Dynamics, and Materials Conference*, AIAA Paper 2018-1912, 2018. https://doi.org/10.2514/6.2018-1912

[19] Blumenthal, B. T., Elmiligui, A. A., Geiselhart, K. A., Campbell, R. L., Maughmer, M. D., and Schmitz, S., "Computational Investigation of a Boundary-Layer-Ingestion Propulsion System," *Journal of Aircraft*, Vol. 55, No. 3, 2018, pp. 1141–1153. https://doi.org/10.2514/1.C034454

[20] Gray, J. S., Mader, C. A., Kenway, G. K. W., and Martins, J. R. R. A., "Modeling Boundary Layer Ingestion Using a Coupled Aeropropulsive Analysis," *Journal of Aircraft*, Vol. 55, No. 3, 2018, pp. 1191–1199. https://doi.org/10.2514/1.C034601

[21] Atinault, O., Carrier, G., Grenon, R., Verbecke, C., and Viscat, P., "Numerical and Experimental Aerodynamic Investigations of Boundary Layer Ingestion for Improving Propulsion Efficiency of Future Air Transport," *31st AIAA Applied Aerodynamics Conference*, AIAA Paper 2013-2406, 2013. https://doi.org/10.2514/6.2013-2406

[22] Kob, L. L., Doherty, J. J., Birch, D. M., and Robson, J., "Experimental and Computational Investigation for In-Line Boundary Layer Ingestion," *AIAA Aviation*, AIAA Paper 2019-3037, 2019. https://doi.org/10.2514/6.2019-3037

[23] "A Method for Estimating Drag-Rise Mach Number at Zero Incidence of Smooth or Bumpy Non-Ducted Axisymmetric Bodies Without or with Fins," IHS Engineering Sciences Data Unit TR 74013, 1974.

[24] Drew, B., and Jenn, A., "Pressure Drag Calculations on Axisymmetric Bodies of Arbitrary Moldline," *28th Aerospace Sciences Meeting*, AIAA Paper 1990-0280, 1990. https://doi.org/10.2514/6.1990-280

[25] Purvis, J. W., and Burkhalter, J. E., "Prediction of Critical Mach Number for Store Configurations," *AIAA Journal*, Vol. 17, No. 11, 1979, pp. 1170–1177. https://doi.org/10.2514/3.7617

[26] Serpieri, J., "Cross-Flow Instability: Flow Diagnostics and Control of Swept Wing Boundary Layers," Ph.D. Thesis, Delft Univ. of Technology, Delft, The Netherlands, 2018, https://doi.org/10.4233/uuid:3dac1e78-fcc3-437f-9579-048b74439f55

[27] Della Corte, B., van Sluis, M., and Gangoli Rao, A., *Results of Overall Configuration Wind Tunnel Testing*, CENTRELINE Public Deliverable D3.02, 2021.

[28] Della Corte, B., Perpignan, A. A., van Sluis, M., and Gangoli Rao, A., "Experimental and Computational Analysis of Model–Support Interference in Low-Speed Wind-Tunnel Testing of Fuselage-Boundary-Layer Ingestion," *9th EASN International Conference*, European Aeronautics Science Network (EASN), Paper 02020, 2019. https://doi.org/10.1051/matecconf/201930402020

[29] Scarano, F., and Riethmuller, M. L., "Iterative Multigrid Approach in PIV Image Processing with Discrete Window Offset," *Experiments in Fluids*, Vol. 26, No. 6, 1999, pp. 513–523. https://doi.org/10.1007/s003480050318

[30] Wieneke, B., "PIV Uncertainty Quantification from Correlation Statistics," *Measurement Science and Technology*, Vol. 26, No. 7, 2015, Paper 074002. https://doi.org/10.1088/0957-0233/26/7/074002

[31] Van Oudheusden, B. W., "PIV-Based Pressure Measurement," *Measurement Science and Technology*, Vol. 24, No. 3, 2013, Paper 032001. https://doi.org/10.1088/0957-0233/24/3/032001

[32] White, F., *Viscous Fluid Flow*, McGraw–Hill, New York, 2006, p. 582, Appendix B.

[33] Ragni, D., Van Oudheusden, B. W., and Scarano, F., "3D Pressure Imaging of an Aircraft Propeller Blade-Tip Flow by Phase-Locked Stereoscopic PIV," *Experiments in Fluids*, Vol. 52, No. 2, 2012, pp. 463–477. https://doi.org/10.1007/s00348-011-1236-6

[34] Sinnige, T., Della Corte, B., De Vries, R., Avallone, F., Merino-Martínez, R., Ragni, D., Eitelberg, G., and Veldhuis, L. L. M., "Alleviation of Propeller-Slipstream-Induced Unsteady Pylon Loading by a Flow-Permeable Leading Edge," *Journal of Aircraft*, Vol. 56, No. 3, 2019, pp. 1214–1230. https://doi.org/10.2514/1.C035250

[35] Brune, G. W., "Quantitative Low-Speed Wake Surveys," *Journal of Aircraft*, Vol. 31, No. 2, 1994, pp. 249–255. https://doi.org/10.2514/3.46481

[36] Maskell, E., "Progress Towards a Method for the Measurement of the Components of the Drag of a Wing of Finite Span," Royal Aircraft Establishment TR 72232, 1972.

[37] Uranga, A., Drela, M., Greitzer, E., Titchener, N., Lieu, M., Siu, N., Huang, A., Gatlin, G. M., and Hannon, J., "Preliminary Experimental Assessment of the Boundary Layer Ingestion Benefit for the D8 Aircraft," *52nd Aerospace Sciences Meeting*, AIAA Paper 2014-0906, 2014. https://doi.org/10.2514/6.2014-0906

F. N. Coton
Associate Editor